Available online at www.sciencedirect.com
SCIENCE DIRECT®
Journal of Magnetic Resonance 166 (2004) 236–245
JMR Journal of Magnetic Resonance
www.elsevier.com/locate/jmr

AIR-SPAMM: alternative inversion recovery spatial modulation of magnetization for myocardial tagging

Anthony H. Aletras,[a,*] Raisa Z. Freidlin,[a,b] Gil Navon,[a,c] and Andrew E. Arai[a]

[a] *Laboratory of Cardiac Energetics, National Heart, Lung and Blood Institute, National Institutes of Health, Building 10, Room B1D416, MSC 1061, Bethesda, MD 20892-1061, USA*
[b] *US Department of Health and Human Services, Center for Information Technology, National Institutes of Health, Bethesda, MD, USA*
[c] *School of Chemistry, Tel Aviv University, Ramat Aviv, Tel Aviv, Israel*

Received 9 June 2003; revised 23 October 2003

Abstract

Alternate inversion recovery spatial modulation of magnetization (AIR-SPAMM) can be used either for doubling the number of tags for a given tagging encoding gradient strength or for improving tagging contrast ratio. AIR-SPAMM requires only a single acquisition and utilizes inversion pulses spaced throughout the gradient recalled echo (GRE) cine acquisition to "lock" the recovering magnetization at a desired level. The theory of AIR-SPAMM is presented along with simulations and results from phantoms. AIR-SPAMM can be used either for imaging systole as demonstrated by initial in vivo results or potentially for imaging the entire cardiac cycle in a slice-interleaved manner.

Keywords: Cardiac; Function; SPAMM; DENSE; Tagging; Heart; MRI; HARP

1. Introduction

Myocardial tagging MRI methods have been available for more than a decade for evaluating cardiac motion and strain [1,2]. With such methods, the image contrast is altered so as to introduce either bands or a grid of signal voids in the myocardium at the beginning of the cardiac cycle. Subsequently, these signal-void patterns are imaged over time as they deform with the contracting myocardium. A qualitative assessment of motion and regional contractility can be easily obtained visually by observing the degree of deformation of the tagging pattern. Quantitative assessment is more tedious and involves user-assisted tag tracking over multiple cardiac phases [3].

The first implementation of a tagging pattern was accomplished with direct saturation of bands orthogonal to the imaging plane [2,4]. This approach was limited by the saturation profile and the number of tagging bands that could be applied within a short amount of time. Spatial modulation of magnetization (SPAMM) was introduced by Axel and Dougherty to overcome these limitations [1]. With SPAMM, the magnetization is brought to the transverse plane where it acquires phase linearly proportional to its position by means of a gradient pulse. The imaginary part of the transverse magnetization is discarded while the real part is stored along the longitudinal axis with its amplitude being sinusoidally modulated across space. This is a result of both the acquired linear phase and the loss of the imaginary part of the magnetization. This sinusoidal modulation results in spatially varying signal voids when the stored longitudinal magnetization is recalled for imaging throughout the cardiac cycle. A variant of the initial SPAMM method includes improved modulation schemes via higher order binomial RF schemes to create a rectangular tagging pattern [5].

The detection of the SPAMM myocardial tagging pattern for quantitative analysis is hindered by tag contrast deterioration throughout the cardiac cycle. The sinusoidal modulation, which gives rise to the tagging signal voids, decays according to T_1, thus, reducing the peak-to-peak amplitude of the tags in the image over

* Corresponding author. Fax: 1-301-402-2389.
E-mail address: Anthony_Aletras@nih.gov (A.H. Aletras).

1090-7807/$ - see front matter © 2003 Elsevier Inc. All rights reserved.
doi:10.1016/j.jmr.2003.10.021

time. The relaxed magnetization, which is restored along the longitudinal axis, results in a background image that lacks the tagging pattern. When imaging early cardiac phases, the tag-modulated component of the image is strong and the non-modulated component is weak. At later cardiac phases the situation is eventually reversed. As a result, the initial signal-voids are offset away from zero by the progressively recovering background component. This can complicate tag detection especially with a receive coil that has an inhomogeneous B_1.

CSPAMM was introduced by Fischer et al. [6] in order to suppress the background component and improve myocardial tagging contrast. With this approach, two RF phase cycled acquisitions are performed orthogonal to each other by storing the sinusoidally modulated magnetization either along $+z$ or $-z$. As such, a positive tagging pattern is collected in the first acquisition while a negative pattern is collected in the second. The background component, which is not dependent on RF cycling, is recovering along $+z$ in both acquisitions. When the two acquisitions are subtracted, the background component is suppressed and the tagging patterns add constructively assuming that otherwise the two acquisitions are identical. This suppression results in improved tagging contrast since the signal voids are no longer offset away from zero due to the background component. However, even though breath-held MRI is commonly performed, the assumption of identical otherwise acquisitions is not always true due to motion. This is particularly true if two breath-holds are required. In cases where the improved contrast is needed for imaging part of the cardiac cycle within a single breath-hold, other alternatives have to be sought.

Another factor contributing to the tagging pattern signal loss over the cardiac cycle is intravoxel dephasing. The generation of signal in SPAMM is the result of generating stimulated echoes as has been previously described by Derbyshire et al. [7]. Therefore, signal loss incurred in the sinusoidally encoded part of the SPAMM signal is a result of intravoxel dephasing, which occurs as the myocardium deforms over the cardiac cycle. At endsystole where the peak of contractile action exists, the pixel size dimensions are maximally altered. As such, the tagging pattern gets distorted due to the local and unpredictable signal loss [8]. Such an effect is the result of strong position encoding gradient pulses during the SPAMM preparation and as such it gets amplified when small tag spacing is used in conjunction with a large pixel size.

We propose alternative inversion recovery SPAMM (i.e., AIR-SPAMM), a method for doubling the number of tags across the field of view without increasing the tagging encoding gradient strength, which results in intravoxel-induced tag signal loss. Also, AIR-SPAMM can be used for improving contrast in tagged images. AIR utilizes multiple inversion pulses interspersed throughout the multiphase SPAMM acquisition in order to "lock" the background component about a desired value.

2. Theory

The magnetization at time zero (M_0), which is stored along the longitudinal axis immediately following a SPAMM preparation (Fig. 1A), was described by Kuijer [9] and is given by

$$M_0 = M_{\mathrm{FID},0} + M_{\mathrm{SINE},0}. \tag{1}$$

Therefore, the stored longitudinal magnetization contains an unmodulated ($M_{\mathrm{FID},0}$) and a spatially sinusoidally modulated ($M_{\mathrm{SINE},0}$) term. $M_{\mathrm{FID},0}$ is given by

$$M_{\mathrm{FID},0} = M_\infty \cos^2\theta \tag{2}$$

and $M_{\mathrm{SINE},0}$ is given by

$$M_{\mathrm{SINE},0} = M_\infty \sin^2\theta\left(\frac{\mathrm{e}^{\mathrm{i}kx+\varphi_1} + \mathrm{e}^{-\mathrm{i}kx-\varphi_1}}{2}\right), \tag{3}$$

where M_∞ is the initial net longitudinal magnetization (which is assumed to be fully relaxed), θ is the tagging flip angle of each of the two SPAMM RF pulses, $kx + \varphi_1$ is the phase imparted by the SPAMM position-encoding gradient, k corresponds to the spatial frequency of the tag lines and φ_1 determines the phase at $x = 0$.

Typically, θ is set at 45° and therefore Eqs. (2) and (3) become, respectively,

$$M_{\mathrm{FID},0} = \frac{M_\infty}{2} \tag{4}$$

and

$$M_{\mathrm{SINE},0} = \frac{M_\infty}{2}\left(\frac{\mathrm{e}^{\mathrm{i}kx+\varphi_1} + \mathrm{e}^{-\mathrm{i}kx-\varphi_1}}{2}\right). \tag{5}$$

In this case, where $\theta = 45°$, the magnetization oscillates sinusoidally between 0 and $+M_\infty$. This is the result of the existing DC offset, which is added by $M_{\mathrm{FID},0}$ Therefore, the tags correspond to zero signal intensity in the image, i.e., to the "valleys" of the sinusoid. Also, since magnitude images are commonly acquired and sign information in lost, this scheme allows the sinusoidal modulation to be correctly depicted in the images since it contains positive magnetization values only.

If a tagging angle of $\theta = 90°$ per RF pulse is applied then Eqs. (2) and (3) become, respectively,

$$M_{\mathrm{FID},0} = 0 \tag{6}$$

and

$$M_{\mathrm{SINE},0} = M_\infty\left(\frac{\mathrm{e}^{\mathrm{i}kx+\varphi_1} + \mathrm{e}^{-\mathrm{i}kx-\varphi_1}}{2}\right). \tag{7}$$

In this case, where $\theta = 90°$, the magnetization oscillates sinusoidally between $-M_\infty$ and $+M_\infty$ since the DC offset is now absent and the entire magnetization is

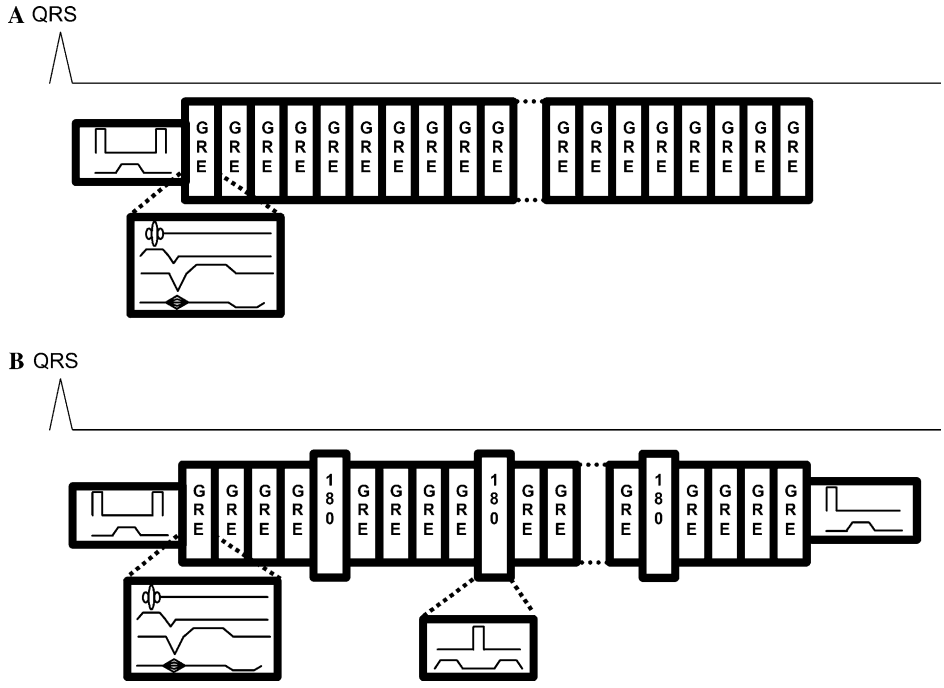

Fig. 1. (A) Schematic diagram of conventional SPAMM pulse sequence with gradient recalled echo readouts. Tagging is performed as soon as the *R*-wave of an EKG is detected. (B) Schematic diagram of the AIR-SPAMM pulse sequence with gradient recalled echo readouts. The AIR inversion RF pulses are followed by crusher gradient pulses, which are not shown here. At the end of the AIR-SPAMM acquisition, the longitudinal magnetization is crushed.

modulated. When magnitude images are considered, this results in rectification of the sinusoidal pattern and therefore the frequency of the tagging pattern is doubled [6]. It is interesting to note that (7) describes also a typical preparation for a stimulated echo phase-based experiments [7,10]. (7) represents magnetization that contains its complex conjugate. Also, the twofold signal loss incurred with stimulated echoes is shown.

As time elapses from the tagging preparation, longitudinal relaxation as a function of time t occurs according to

$$M(t) = M_\infty + [M_0 - M_\infty]\mathrm{e}^{-t/T_1}, \tag{8}$$

where M_∞ is the magnetization following full longitudinal relaxation. Substitution of M_0 from Eq. (1) into Eq. (8) yields the longitudinal magnetization at any time after the SPAMM preparation to be

$$M(t) = M_{\mathrm{FID}}(t) + M_{\mathrm{SINE}}(t), \tag{9}$$

where

$$M_{\mathrm{FID}}(t) = M_\infty + [M_{\mathrm{FID},0} - M_\infty]\mathrm{e}^{-t/T_1} \tag{10}$$

and

$$M_{\mathrm{SINE}}(t) = M_{\mathrm{SINE},0}\mathrm{e}^{-t/T_1}. \tag{11}$$

Eq. (10) describes how the unmodulated longitudinal component of the magnetization, M_{FID} recovers along the z-axis while (11) shows how the sinusoidally modulated component, M_{SINE} decays. Both exponential processes follow the same time constant, T_1 It is interesting to note that because they both follow the same exponential constant, it is guaranteed that, if $\theta = 45°$ (Eqs. (4) and (5)), the modulated term will always be positive and therefore will not be ill-rectified at any time if magnitude images are collected throughout the cardiac cycle. However, the recovery of M_{FID} results in reduced tagging contrast [6] as time elapses since the valleys of the sine pattern are no longer at zero.

Any multiphase imaging method that is utilized to map the tagged magnetization throughout the cardiac cycle will further deplete both M_{FID} and M_{SINE} and will therefore contribute to a reduced tagging contrast as time elapses. Depending on the readout flip angle, M_{FID} can reach a steady-state but M_{SINE} will always be depleted. The effects of the selected sequence parameters can be significant with respect to the contrast obtained since the tagged images are acquired over several heartbeats [11]. A commonly utilized readout for tagging is that of a multiphase gradient echo, which is shown in Fig. 1A [12].

To maintain tagging contrast, AIR inversion pulses are applied at the end of every interval τ, where τ is a multiple of TRs of the gradient echo readout used in SPAMM imaging. In practice, τ is set equal to the temporal resolution of the multiphase cardiac acquisition. The effect of these inversion pulses on the longitudinal magnetization can be better understood if observed during two such consecutive intervals, i.e., 2τ.

The magnetization (Eq. (9)) at the end of the first τ interval is

$$M(\tau) = \underbrace{M_\infty + [M_{\mathrm{FID},0} - M_\infty]e^{-\tau/T_1}}_{\mathrm{FID}} + \underbrace{M_{\mathrm{SINE},0}e^{-\tau/T_1}}_{\mathrm{SINE}}. \quad (12)$$

The ensuing inversion pulse inverts the sign of M(τ) and therefore at the end of the second τ interval the sinusoidal component is

$$M(2\tau) = \underbrace{-M_{\mathrm{FID},0}e^{-2\tau/T_1} \overbrace{+M_\infty\left[1 - 2e^{-\tau/T_1} + e^{-2\tau/T_1}\right]}^{\mathrm{RES}}}_{\mathrm{FID}} \underbrace{-M_{\mathrm{SINE},0}e^{-2\tau/T_1}}_{\mathrm{SINE}}. \quad (13)$$

This residual term RES is approximately zero as can be shown by Taylor series expansion of its terms. The error in this approximation is of the order of $(\tau/T_1)^2$. Since $\tau \approx 40$ ms and $T_1 = 850$ ms for the myocardium, this error is less than 0.003. Therefore, Eq. (13) is approximated by

$$M(2\tau) = \underbrace{-M_{\mathrm{FID},0}e^{-2\tau/T_1}}_{\mathrm{FID}} \underbrace{-M_{\mathrm{SINE},0}e^{-2\tau/T_1}}_{\mathrm{SINE}}. \quad (14)$$

Eq. (14) shows that in an AIR-SPAMM experiment where the FID and SINE components start at the same amplitude following the tagging preparation (i.e., $\theta = 45°$, Eqs. (4) and (5)), as time elapses the FID and SINE track each other with respect to their amplitudes. On the other hand, if the FID starts at zero (i.e., $\theta = 90°$, Eqs. (6) and (7)), it will oscillate about zero with a period of 2τ. Thus, in both cases, if the sign of the magnetization is not considered, the AIR-SPAMM inversion pulses "lock" the FID magnetization about its initial value M_0. Each inversion pulse results in conjugation of the existing SINE magnetization, i.e., it changes the sign of the sinusoidal pattern. Since magnitude images are reconstructed, this does not affect the resulting image. However, for any cardiac phase, if k space is filled from acquisitions straddling AIR inversion pulses then the appropriate conjugation has to be applied prior to Fourier transformation.

AIR-SPAMM is well suited for using a progressively higher GRE flip angle as data are sampled throughout systole in order to equally distribute the available sinusoidally modulated magnetization across the systolic cardiac phases. This has been previously described by Fischer et al. [13].

3. Methods

Simulations of the tagging experiment were performed and the effect of the inversion pulses in AIR-SPAMM was studied. The tagging preparation (Eqs. (1)–(3)) described in Section 2 were simulated in IDL (Research Systems, Boulder, CO) and applied to an axial slice of a simulated spherical phantom with a T_1 of 850 ms, i.e., equal to that of normal myocardium. The longitudinal magnetization was tracked every 1ms. In order to demonstrate the underlying process, the GRE flip angle was simulated at 1°. This ensured that the readout scheme itself would not significantly deplete the SINE component. Simulations [9] for both SPAMM and AIR-SPAMM were also performed to examine the effects of intravoxel dephasing to the tagging pattern. These simulations were evaluated against in vivo data acquired from a canine experiment.

All experiments were performed with a General Electric Medical Systems (Waukesha, WI) 1.5 T cardiovascular magnet. Phantom data were acquired with the standard birdcage head resonator. The T_1 of the cylindrical phantom (3% agar in saline doped with $CuSO_4$) was 720 ms. The human experiment was done with a standard four-element receive-only phased array coil. Similar imaging parameters were used for both types of experiments.

For conventional tagging, the 1-1 SPAMM preparation was applied immediately following the *R*-wave of the EKG. The tagging angle for each of the two RF pulses was either $\theta = 45°$ or $\theta = 90°$ as noted. The tagging gradient area was adjusted for a tag wavelength of 7 pixels. Since magnitude images were acquired and the tagging waveform was rectified in some experiments, this occasionally resulted in a tags with spacing of 3.5 pixels and a tagging profile very similar to a 1-2-1 SPAMM preparation [6]. For quantitative analysis, images with a larger tag spacing (wavelength of 30 pixels) were also acquired. The entire tagging preparation lasted approximately 9.8 ms. GRE multiphase imaging followed the SPAMM preparation in order to map cardiac motion. The following parameters were used: 3-lobe sinc RF pulse 0.6 ms long, flip angle 10°, field of view 36×28 cm, slice thickness 8 mm, bandwidth ± 62.5 kHz, echo time (TE) 2.2 ms, repetition time (TR) 4.9 ms, data matrix of 256×120. The temporal resolution was 39.2 ms since eight consecutive k-space lines (views) were ascribed to each cardiac phase imaged (views-per-segment 8). Therefore, the total acquisition time was 16 heartbeats. An interleaved k-space sampling scheme was applied to smooth transitions in the k_Y direction. With this type of interleaving, views were grouped according to their acquisition order in k-space.

For AIR-SPAMM acquisitions, additional non-slice-selective inversion pulses to suppress the FID were inserted every 8 TRs in a synchronous manner to the cardiac-phase time boundaries. The inversion pulse duration was 0.5 ms. In order to avoid the creation of stimulated and/or spin echoes by any imperfection of these inversions, crusher gradients were applied immediately following each RF pulse with an area of 3240 μs G/cm along all three axes. To ensure proper crushing, the sign of

the gradient pulse along X was changed every two inversions, along Y every four inversions, and along Z every eight inversions. To avoid stimulated echoes across heartbeats, at the end of the systolic data acquisition with AIR-SPAMM a 90° RF pulse and a gradient crusher pulse were applied (Fig. 1). Progressively higher GRE flip angles during readout [13] were used for both SPAMM and AIR-SPAMM acquisitions.

Image reconstruction was performed with the standard software available on the magnet system. For estimating tagging contrast difference (CD) and contrast difference ratio (CDR), signal intensity (SI) profiles perpendicular to the tagging pattern were analyzed in the phantom images acquired with a tag spacing of 30 pixels. Four pixels at the minimum SI of one valley as well as four pixels at the maximum SI of one top were averaged to yield, respectively, the minimum (I_{VALLEY}) and maximum (I_{TOP}) values of the tagging SINE in each profile. CD and CDR were computed according to Eqs. (15) and (16), respectively,

$$\mathrm{CD} = I_{\mathrm{TOP}} - I_{\mathrm{VALLEY}}, \tag{15}$$

$$\mathrm{CDR} = \frac{I_{\mathrm{TOP}} - I_{\mathrm{VALLEY}}}{I_{\mathrm{VALLEY}}}. \tag{16}$$

4. Results

Fig. 2 shows a simulation of k-space and magnitude images for conventional SPAMM and AIR-SPAMM at 0 and 300 ms after a 1-1 preparation with either $\theta = 45°$ or $\theta = 90°$. Note that changing the tagging angle per pulse from 45° (Fig. 2A) to 90° (Fig. 2B) effectively doubles the tag density at $t = 0$ ms. However, with $\theta = 90°$ the tag density decreases atmost by half by $t = 330$ ms even though this is a static, non-deforming phantom. AIR-SPAMM also effectively doubles the tag density when going from $\theta = 45°$ (Fig. 2C) to $\theta = 90°$ (Fig. 2D). However, this occurs not only at time $t = 0$ ms but consistently throughout systole (Fig. 2D). These simulations also depict, in a qualitative manner, the CDR between tagged and untagged tissue, which diminishes as time passes with conventional SPAMM with $\theta = 45°$ (Fig. 2A). The corresponding AIR-SPAMM (Fig. 2C) preserves CDR across systole as seen by the consistently dark tagged lines. Fig. 3 shows the time intensity curves for the FID (solid) and SINE (dotted) components of the magnetization for SPAMM and AIR-SPAMM simulated data presented in Fig. 2. For AIR-SPAMM, Fig. 3C shows how the FID and

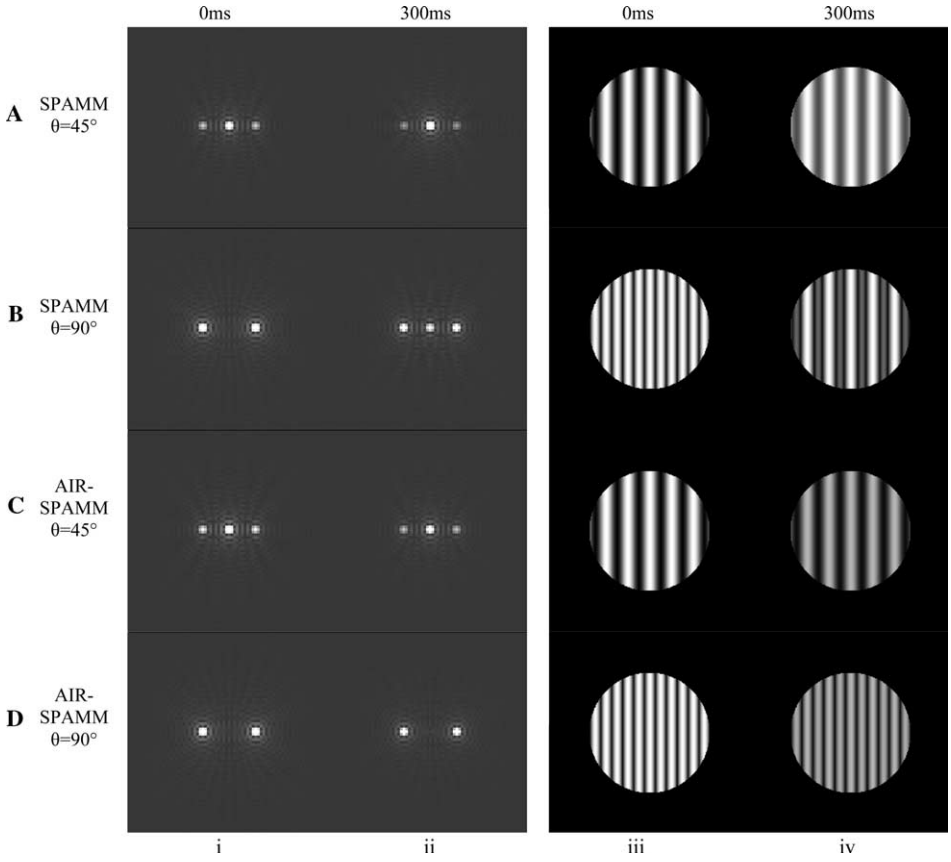

Fig. 2. Simulated k-space matrices (columns i and ii) and simulated magnitude phantom images (columns iii and iv) immediately following tagging preparation (columns i and iii) and 300 ms later (columns ii and iv). SPAMM data with $\theta = 45°$ and $\theta = 90°$ are shown in rows A and B, respectively. Simulated AIR-SPAMM data with $\theta = 45°$ and $\theta = 90°$ are shown in rows C and D, respectively.

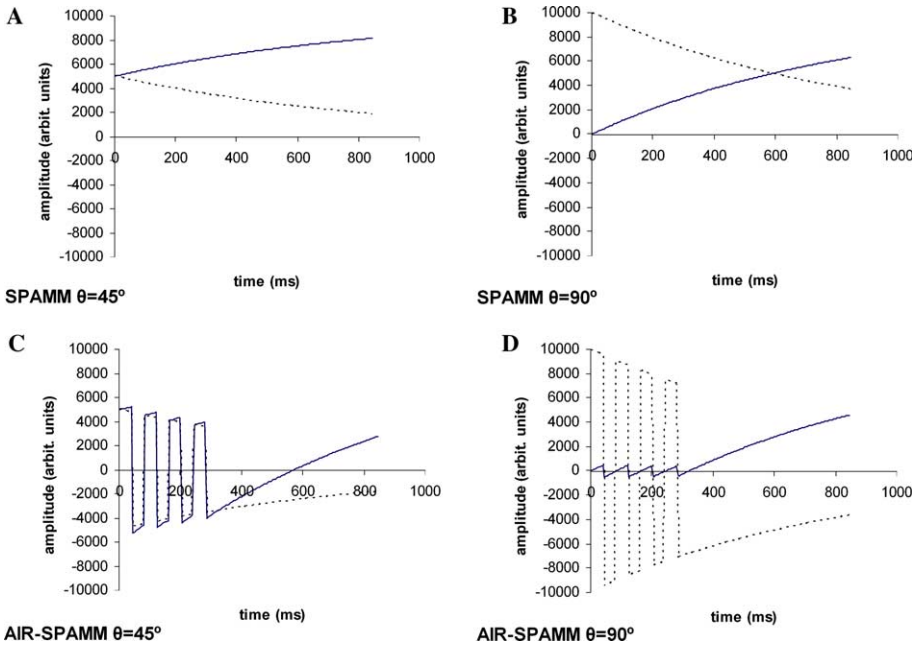

Fig. 3. (A) Simulated SPAMM ($\theta = 45°$) signal recovery of the FID (solid line) and decay of the SINE modulated component (dotted line) of the longitudinal magnetization. (B) Simulated SPAMM ($\theta = 90°$). (C) Simulated AIR-SPAMM ($\theta = 45°$). Note that the two signals track with each other while the inversion pulses are played out during the first 300 ms. (D) Simulated AIR-SPAMM ($\theta = 90°$). Note that the FID is ''locked'' about zero while the inversion pulses are played out.

SINE track with each other when $\theta = 45°$ while Fig. 3D shows how the FID is ''locked'' close to zero when $\theta = 90°$. Fig. 4 shows the time evolution (0, 150, and 300 ms) of the horizontal signal profile at mid-level of the simulated phantom shown in columns iii and iv of Fig. 2. When using $\theta = 45°$, note the difference over time between SPAMM (first row) and AIR-SPAMM (third row) with respect to signal nulling within the tag valleys. Also, when $\theta = 90°$, note that SPAMM (second row) yields variable tag spacing, which renders this implementation useless. In contrast, AIR-SPAMM (last row) results in double density tags of fixed spacing.

Fig. 5 shows phantom images acquired with conventional SPAMM and AIR-SPAMM with either

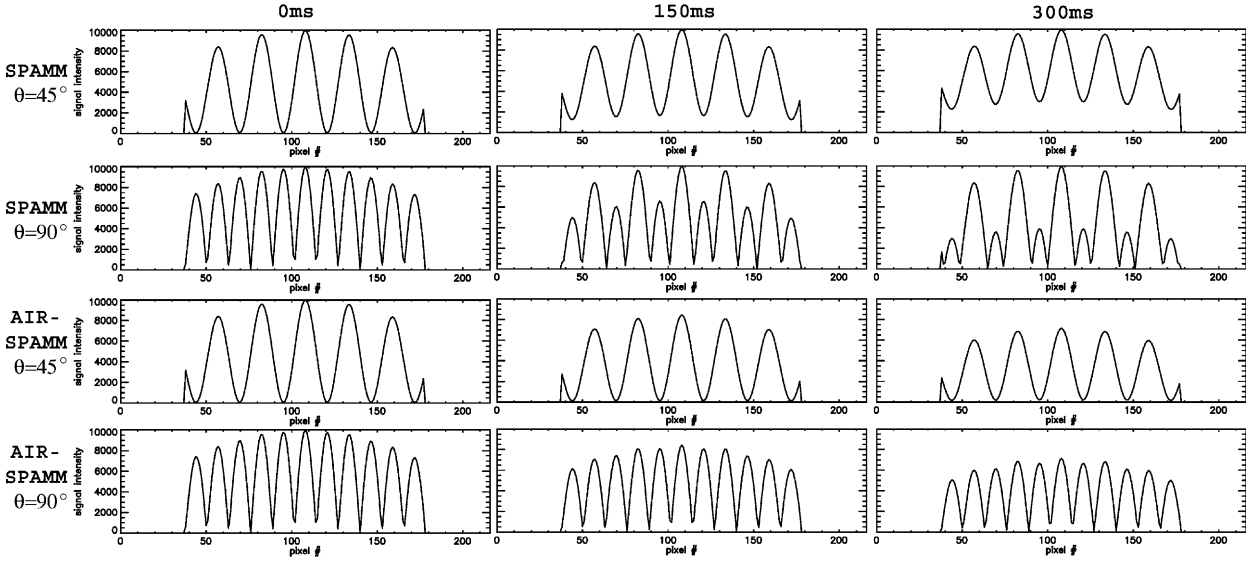

Fig. 4. Signal intensity profiles over three time points (0, 150, and 300 ms) for the simulated images shown in Fig. 2. Note that when using SPAMM with $\theta = 45°$ (first row) the tag valleys are not consistently at zero over time in contrast to using AIR-SPAMM with $\theta = 45°$ (third row) where the valleys are always at zero. When SPAMM is used with with $\theta = 90°$ (second row) the recovery of the FID results in variable tag spacing over time for this motionless object. AIR-SPAMM with $\theta = 90°$ (last row) results in consistent double density tags over time.

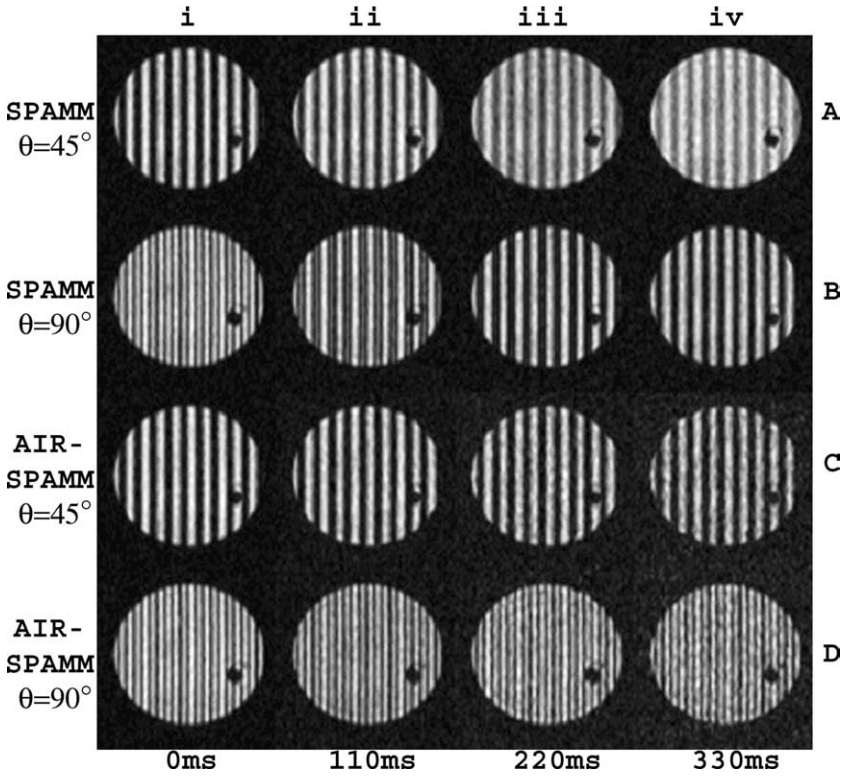

Fig. 5. Even set of four (out of eight) acquired images acquired equitemporaly during 330 ms (columns i–iv, respectively) following the tagging preparation. Conventional SPAMM with $\theta = 45°$ and $\theta = 90°$ (rows A and B, respectively) and AIR-SPAMM with $\theta = 45°$ and $\theta = 90°$ (rows C and D, respectively) are shown. Note that with $\theta = 45°$ AIR-SPAMM (C-iv) results in consistent suppression of the non-tagged background relative to SPAMM (A-iv). Also, that with $\theta = 90°$ AIR-SPAMM (D-iv) results in correct tag spacing, whereas with SPAMM (B-iv) tag spacing is half of what was initially observed (B-i). The circular void observed in the phantom is an air pocket, which acts as a spatial marker.

$\theta = 45°$ or $\theta = 90°$ over 330 ms (every other acquired image is shown). The same observations with respect to tag density and contrast can be made as with Fig. 2, when comparing the two methods. CD and CDR for SPAMM and AIR-SPAMM with $\theta = 45°$ are reported in Fig. 6 for each time frame over all its profiles within the phantom as means ± standard deviation. Human images acquired from a normal volunteer over systole to demonstrate improved CDR with AIR-SPAMM ($\theta = 45°$) are shown in Fig. 7.

Fig. 8 shows simulated endsystolic short axis images with SPAMM (top left) and AIR-SPAMM (top right), respectively. Note the tagging pattern blurring at areas of high strain in the SPAMM image (top left, arrow). This effect is not present in the simulated AIR-SPAMM image (top right, arrow). The bottom row of Fig. 8 shows

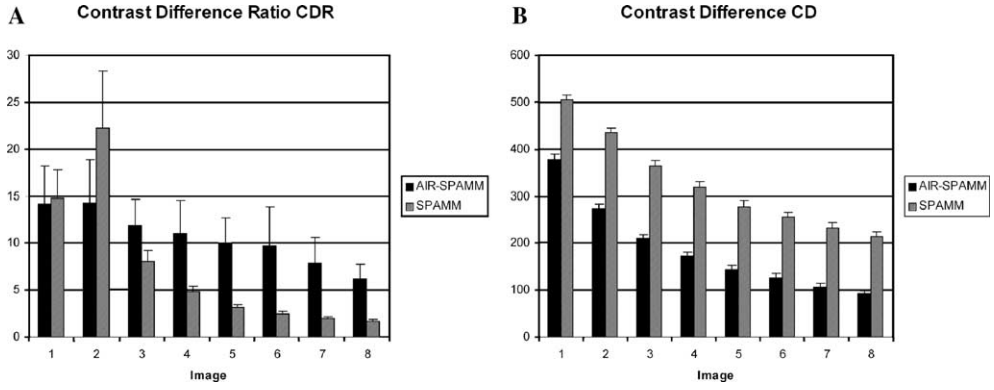

Fig. 6. Contrast difference ratio, CDR (A) and contrast difference, CD (B) measurements from phantom images. With conventional SPAMM ($\theta = 45°$) (stripped gray bars) CD is higher than with AIR-SPAMM ($\theta = 45°$) (solid black bars) as a result of losses described in Section 5. However, CDR is generally higher (images 3–8) with AIR-SPAMM as a result of having the 'valleys' of the tags 'locked' at zero. Error bars correspond to standard deviation (both $p < 0.01$).

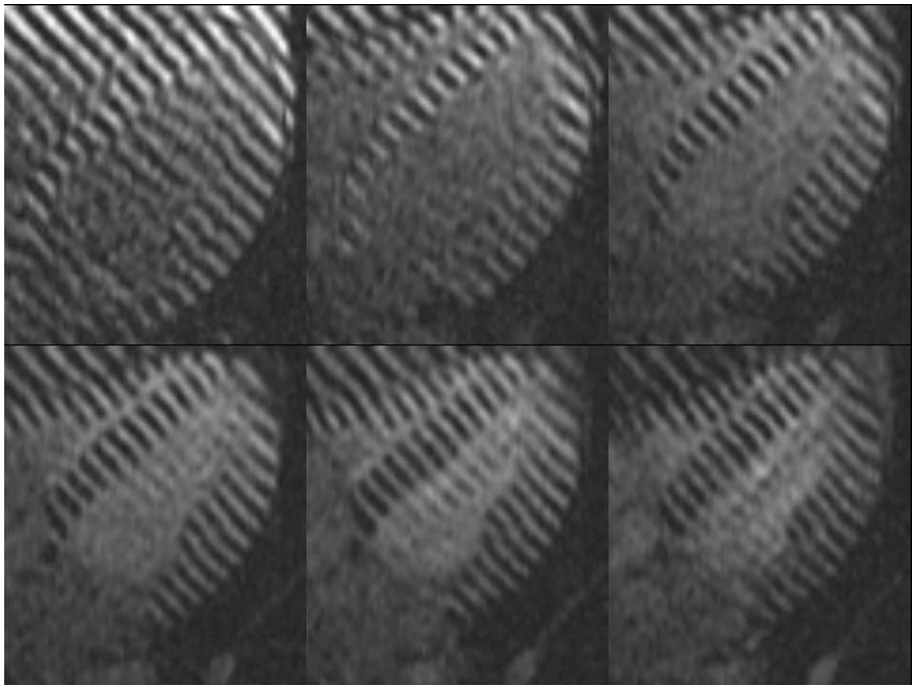

Fig. 7. AIR-SPAMM magnitude images acquired equitemporaly over systole from a normal volunteer. The effective tag spacing was 6 pixels. Progressively higher flip angles were used as described in Section 2 with a nominal T_1 of 850 ms for the myocardium.

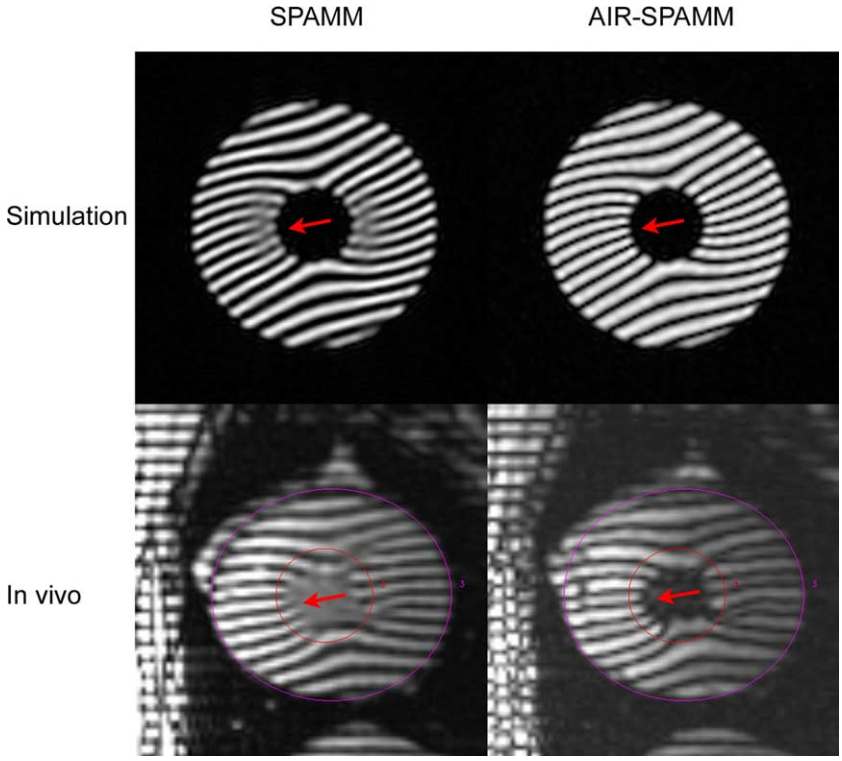

Fig. 8. Simulated (top row) and in vivo (bottom row) images with SPAMM (left column) and AIR-SPAMM (right column) show that the tag fading and blurring with SPAMM due to intravoxel dephasing in areas of high stain (left column, arrows) is not present in AIR-SPAMM images (right column, arrows). The in vivo images have identical circular regions delineated so as to define the epicardial surface and about 1 mm away from the endocardium. With SPAMM, intravoxel dephasing causes blurring and loss of the tagging pattern (arrow). With AIR-SPAMM, the endocardium is more distinctly visualized.

similar data from images obtained in vivo. In vivo, where strain is highest in the subendocardium, tag blurring is seen with SPAMM (bottom left, arrow) while the same heart shows more distinct tagging patterns in the same region with AIR-SPAMM (bottom right, arrow).

5. Discussion

AIR-SPAMM can be used either for doubling the number of tags for a given tagging encoding gradient strength or for improving tagging CDR.

When AIR-SPAMM is used for acquiring tagged images with double tag density, the goal is FID suppression. Then, it is possible to properly rectify the sinusoidal waveform via magnitude reconstruction and acquire images with a consistent doubled tag density, as described in Section 2. If conventional SPAMM is used with a tagging angle of $\theta = 90°$ then the entire magnetization is utilized and the sinusoidal modulation is in the range of $-M_Z$ to $+M_Z$ With magnitude reconstruction, the rectification of the sinusoidal waveform, in early times following the tagging preparation, results in the doubling of the tagging frequency (Fig. 5B). Here, the tag lines coincide with the zero-crossings of the sine waveform (Fig. 5Bi). As T_1 relaxation sets in, less and less of the sine gets improperly rectified since a progressively rising DC offset (i.e., the recovering FID) is added to it (Fig. 5Biv). This results in a variable tagging spacing with conventional SPAMM as time elapses even in the absence of phantom motion or deformation (Fig. 4, second row). This essentially renders SPAMM useless with a tagging flip angle of $\theta = 90°$ and magnitude reconstruction. When AIR-SPAMM is applied with $\theta = 90°$, the initial SINE waveform is bracketed by $\pm M_Z$ (Fig. 3D). The AIR inversion pulses keep the FID magnetization "locked" about $z = 0$ (Fig. 3D, solid line). Here, the zero crossings of the sine modulation correspond to the tagging signal voids (Fig. 5D) throughout time therefore resulting in consistent double density tags (Fig. 4, last row). This increased tag density with AIR-SPAMM is achieved without the need to increase the strength of the tagging gradient (Fig. 1). As a result, for a given pixel size, the intravoxel dephasing incurred by the sinusoidal pattern is reduced as its components fall within the sampled k-space area [8]. This is visible in areas of high strain, such as the endocardium, in both simulated and in vivo data (Fig. 8). Even in non-extreme cases such as the latter, AIR-SPAMM always shifts in k-space the high frequency content of the SINE components by half when compared to SPAMM. As such, it has potential to result in a more defined tagging pattern, which should be easier to track via software [14].

In its alternative implementation, AIR-SPAMM with a tagging flip angle of $\theta = 45°$ results in improved CDR. With conventional SPAMM ($\theta = 45°$) the FID contributes to the overall image as a background unmodulated GRE image, which degrades CDR as time elapses from the tagging preparation (Fig. 4, first row). The inversion pulses in AIR-SPAMM cause equal amounts of signal to be contributed to the image from the FID and the SINE throughout systole (Fig. 3C). In this case, the "valleys" of the sine coincide with zero consistently over time (Figs. 5C and Fig. 4, third row) and therefore they represent consistently dark signal tagging voids. In this manner, tagging CDR is improved without requiring a second acquisition, as is the case with C-SPAMM. This suppression is effective also in the case of highly inhomogeneous receive coil profiles, where windowing and leveling cannot be uniformly applied to visualize the background consistently dark.

The successful imaging of a rectified tagging pattern was introduced originally by Tsekos et al. [15] albeit based on a different premise than that of AIR-SPAMM. In their work, the use of a tandem pair of adiabatic DANTE inversion sequences results in a tagged pattern that is rectified per se and therefore is not dependent on the magnitude reconstruction for the rectification as with AIR-SPAMM. Since the tagging pattern is rectified even before data acquisition begins, the FID longitudinal recovery no longer results in variable tag spacing with their method. However, since the FID recovers, neither the increased CDR nor the intravoxel dephasing insensitivity is present. On the other hand, since their method is based on adiabatic excitation, there is a clear advantage for using it with transmit/receive surface coils that possess highly inhomogeneous B_1.

The suppression of the FID (when $\theta = 90°$) with AIR-SPAMM has implications for imaging that is performed across multiple RR intervals. If imaging persists throughout the entire cardiac cycle then during the subsequent cycle no longitudinal magnetization exists due to the AIR inversion pulses. Thus, imaging cannot commence anew unless sufficient time is allowed to pass for T_1 relaxation to occur. One could potentially image another slice during the subsequent cardiac cycle assuming that the inversion pulses are slab selective and that they track only the slice being imaged at any time. However, this approach results in long breath-holds, similar to those of C-SPAMM, since two slices at least need to be acquired interleaved. The approach taken in this paper was to image with AIR-SPAMM the same slice in consecutive cardiac cycles throughout only systole and allow for T_1 recovery of the FID during diastole. This shortened the breath-hold to 12–16 heartbeats.

When compared to conventional SPAMM, imaging only systole with AIR-SPAMM results in signal loss (approximately 12%) since approximately 300 ms of the cardiac cycle is no longer used for FID recovery. From simulations, if the effect of the GRE flip angle (com-

monly set at 10°) is accounted for then, after the first RR interval, conventional SPAMM tagging samples approximately 41% of the available magnetization. This is a result of the steady-state, which sets in between consecutive cardiac cycles under the assumptions that myocardial T_1 is 850 ms and $\theta = 45°$. Under these conditions, the amount of magnetization sampled during each TR is about 7% of the available maximum.

The AIR RF pulses, which are used with AIR-SPAMM, can result in signal loss for two main reasons. First, any deviation from a perfect 180° RF pulse directly translates in depleting the sinusoidally modulated longitudinal magnetization. As such, the pulse's excitation profile becomes important. It is also crucial to use inversion pulses that are either calibrated to the proper flip angle or that are more insensitive to the calibration itself. Indeed, adiabatic pulses could potentially solve this problem. In practice however, it was determined that the length of the adiabatic pulses (on the order of 3 ms) resulted in attenuation of the sinusoidally modulated signal due to T_2 losses [16]. This second mechanism (i.e., spin–spin interactions) of signal loss prompted the use of non-slice-selective inversion pulses with a short length (0.5 ms). The loss measured from the data as a result of the inversion pulses alone was 12%. The application of a progressively increasing flip angle scheme for the GRE readout results in uniform signal intensity over the phases sampled throughout systole (Fig. 7).

In the described implementation, one AIR inversion was applied for every 8 TRs in a synchronous manner to the cardiac-phase time boundaries. This time interval of approximately 40 ms was dictated by the necessity to keep temporal resolution at a rate acceptable for cardiac imaging. While feasible, applying AIR inversion pulses at a higher rate complicates image reconstruction since the k-space data for a given cardiac phase straddle inversion pulses. Also, as mentioned earlier, T_2 losses incurred during each AIR inversion would accumulate faster and thus degrade image quality. More frequent application of AIR inversion pulses would also raise the specific absorption ratio (SAR). However, in this implementation, even when applied every two TRs average, SAR never exceeded 2 W/kg.

In conclusion, AIR-SPAMM was developed in order to either increase the number of tags or improve contrast in tagging experiments. This method can image systole while keeping at desired levels the unmodulated component of the longitudinal magnetization over time. This type of FID manipulation could also prove to be useful in phase-based motion tracking methods such as DENSE [10] for improving their spatial resolution when used in a multiphase manner.

References

[1] L. Axel, L. Dougherty, MR imaging of motion with spatial modulation of magnetization, Radiology 171 (3) (1989) 841–845.
[2] E.A. Zerhouni, Myocardial tagging by magnetic resonance imaging, Coron. Artery Dis. 4 (4) (1993) 334–339.
[3] A. Bazille, M.A. Guttman, E.R. McVeigh, E.A. Zerhouni, Impact of semiautomated versus manual image segmentation errors on myocardial strain calculation by magnetic resonance tagging, Invest. Radiol. 29 (4) (1994) 427–433.
[4] E.A. Zerhouni, D.M. Parish, W.J. Rogers, A. Yang, E.P. Shapiro, Human heart: tagging with MR imaging—a method for noninvasive assessment of myocardial motion, Radiology 169 (1) (1988) 59–63.
[5] L. Axel, L. Dougherty, Heart wall motion: improved method of spatial modulation of magnetization for MR imaging, Radiology 172 (2) (1989) 349–350.
[6] S.E. Fischer, G.C. McKinnon, S.E. Maier, P. Boesiger, Improved myocardial tagging contrast, Magn. Reson. Med. 30 (2) (1993) 191–200.
[7] J.A. Derbyshire, N.F. Osman, in: Cardiac Motion Encoding using HARP and DENSE: Tagging or Phase Contrast? Glasgow, Scotland, UK, April 21–27, 2001, p. 1875.
[8] V.J. Wedeen, R.M. Weisskoff, B.P. Poncelet, MRI signal void due to in-plane motion is all-or-none, Magn. Reson. Med. 32 (1) (1994) 116–120.
[9] J.P. Kuijer, E. Jansen, J.T. Marcus, A.C. van Rossum, R.M. Heethaar, Improved harmonic phase myocardial strain maps, Magn. Reson. Med. 46 (5) (2001) 993–999.
[10] A.H. Aletras, H. Wen, Mixed echo train acquisition displacement encoding with stimulated echoes: an optimized DENSE method for in vivo functional imaging of the human heart, Magn. Reson. Med. 46 (3) (2001) 523–534.
[11] D.A. Herzka, P. Kellman, A.H. Aletras, M.A. Guttman, E.R. McVeigh, Multishot EPI-SSFP in the heart, Magn. Reson. Med. 47 (4) (2002) 655–664.
[12] E.R. McVeigh, E. Atalar, Cardiac tagging with breath-hold cine MRI, Magn. Reson. Med. 28 (2) (1992) 318–327.
[13] S.E. Fischer, G.C. McKinnon, M.B. Scheidegger, W. Prins, D. Meier, P. Boesiger, True myocardial motion tracking, Magn. Reson. Med. 31 (4) (1994) 401–413.
[14] E. Atalar, E.R. McVeigh, Optimization of tag thickness for measuring position with magnetic resonance imaging, IEEE Trans. Med. Imaging 13 (1) (1994) 152–160.
[15] N.V. Tsekos, M. Garwood, K. Ugurbil, Tagging of the magnetization with the transition zones of 360 degrees rotations generated by a tandem of two adiabatic DANTE inversion sequences, J. Magn. Reson. 156 (2) (2002) 187–194.
[16] S. Michaeli, M. Garwood, X.H. Zhu, L. DelaBarre, P. Andersen, G. Adriany, H. Merkle, K. Ugurbil, W. Chen, Proton T2 relaxation study of water, *N*-acetylaspartate, and creatine in human brain using Hahn and Carr–Purcell spin echoes at 4 T and 7 T, Magn. Reson. Med. 47 (4) (2002) 629–633.